Phonon and free-charge-carrier properties of $Zn_{1-x}Mn_xSe$ epilayers grown by molecular-beam epitaxy

K. C. Agarwal,* B. Daniel, C. Klingshirn, and M. Hetterich
Institut für Angewandte Physik and Center for Functional Nanostructures (CFN), Universität Karlsruhe, Wolfgang-Gaede-Strasse 1, D-76131 Karlsruhe, Germany

(Received 23 August 2005; revised manuscript received 21 November 2005; published 31 January 2006)

Far infrared and mid infrared (FIR-MIR) reflectivity measurements have been carried out on two different series of undoped and chlorine-doped $Zn_{1-x}Mn_xSe$ epilayers grown by molecular-beam epitaxy. The FIR reflection studies performed upon the series of undoped $Zn_{1-x}Mn_xSe$ samples suggest an intermediate-mode behavior for the optical phonon modes in the composition range ($0 \leqslant x \leqslant 0.43$). In addition to the known ZnSe-like and MnSe-like phonon resonances a "weak-mode" feature is found below the MnSe-like phonon band. The frequency of this feature shows a temperature and Mn dependent redshift. We suggest that this feature originates from the alloy disorder present in the samples. The shape of the reststrahlen band is found to change significantly with layer thickness. This is discussed in some detail for pure ZnSe epilayers. To extract some information about the electron effective mass, we performed room-temperature plasma edge measurements on chlorine-doped *n*-type $Zn_{1-x}Mn_xSe$ epilayers ($0 \leqslant x \leqslant 0.13$). Via Drude-Lorentz-type multioscillator fits to our data, we extracted the optical electron effective mass (m^*_{op}) in a series of doped Zn(Mn)Se:Cl samples with different Mn contents and free-electron concentrations. Our results indicate that m^*_{op} in $Zn_{1-x}Mn_xSe$ is lower than that for ZnSe. In *n*-type chlorine-doped ZnSe samples with different free-electron concentrations, m^*_{op} varied from 0.133 m_0 to 0.152 m_0, while in $Zn_{0.87}Mn_{0.13}Se$:Cl samples, we found a variation from 0.095 m_0 to 0.115 m_0 within about ±9% experimental accuracy. From theoretical calculations, we determined the extrapolated room-temperature band-edge electron mass in ZnSe and $Zn_{0.87}Mn_{0.13}Se$ to be about 0.132 m_0 and 0.093 m_0, respectively. Additionally, from electrical Hall effect measurements on $Zn_{1-x}Mn_xSe$:Cl epilayers, we found a drastic reduction in the free-electron concentration with increasing Mn content. The incorporation of Mn increases the resistivity and decreases the mobility of the free charge carriers in the samples.

DOI: 10.1103/PhysRevB.73.045211 PACS number(s): 78.30.Fs, 71.20.Nr

I. INTRODUCTION

The large band gap and the close matching of the ZnSe lattice constant to that of GaAs make ZnSe-based materials interesting for a variety of potential applications in optoelectronic devices, e.g., light-emitting diodes and blue-green laser diodes,[1–3] electro-optic waveguide modulators,[4] or blue-ultraviolet photodetectors.[5] $Zn_{1-x}Mn_xSe$ belongs to the group of II-Mn-VI semimagnetic or diluted magnetic semiconductors (DMSs) with an energy gap tunable between 2.66–3.4 eV, depending on the Mn content and the applied magnetic field.[6–8] In $Zn_{1-x}Mn_xSe$, Zn^{2+} ions are randomly substituted by magnetic Mn^{2+} ions in the cation positions, leading to interesting magneto-optical properties, such as a giant Zeeman splitting of the band edges.[6,7,9] The latter makes it a suitable candidate for divising spin filters[10] or utilizing it as a spin aligner in spin-based optoelectronic devices (see, e.g., Refs. 11–14).

In the present work, unpolarized reflection measurements in the far-infrared to the mid-infrared spectral range are employed in combination with electrical Hall effect measurements in order to investigate the phonon and free-charge-carrier properties of $Zn_{1-x}Mn_xSe$ as a function of Mn content and free-electron concentration. Previous reports on long-wavelength optical phonons in bulk and thin film $Zn_{1-x}Mn_xSe$ epilayers investigated via Raman scattering[15–17] and/or using far-infrared reflection and transmission studies[18,19] demonstrated that $Zn_{1-x}Mn_xSe$ exhibits an intermediate-mode behavior for the optical phonons. However, there was only experimental evidence for ZnSe-like and MnSe-like phonon features. To our knowledge, there are no reports available in the literature for the electron effective mass in $Zn_{1-x}Mn_xSe$.[20]

For investigating phonon properties, we used the dielectric response model to analyze our FIR reflection measurements performed on a series of six undoped $Zn_{1-x}Mn_xSe$ samples with different Mn content. Phonon properties and the thickness effect on the reststrahlen region are discussed, based on experimental data and theoretical modeling. The room-temperature plasma edge measurements have been carried out on nine chlorine-doped $Zn_{1-x}Mn_xSe$ samples ($0 \leqslant x \leqslant 0.13$) with different free-electron concentrations. Hall effect measurements were performed on chlorine-doped $Zn_{1-x}Mn_xSe$ samples with various Mn contents ($0 \leqslant x \leqslant 0.30$). We report the effect of Mn on the free-charge-carrier effective mass, free-electron concentration, mobility, and resistivity in differently doped $Zn_{1-x}Mn_xSe$ samples. Results are presented and discussed.

The used experimental techniques and growth of samples are described in Sec. II. The theoretical background for making fits to the infrared reflection data is presented in Sec. III A. In Sec. III B, we discuss the theoretical calculation of the electron effective mass. Section IV A contains our results for the temperature dependence of the zone center optical

phonons in undoped $Zn_{1-x}Mn_xSe$ epilayers with different Mn contents ($0 \leqslant x \leqslant 0.43$). The thickness effects on phonon features are explained in Sec. IV B. Section IV C presents our plasma edge measurements performed on chlorine-doped $Zn_{1-x}Mn_xSe$ epilayers having low Mn content ($0 \leqslant x \leqslant 0.13$). It summarizes and compares results of experimentally obtained optical electron effective mass values with theoretical ones calculated using Kane's two-band model. The conduction band-edge masses for ZnSe and $Zn_{0.87}Mn_{0.13}Se$ obtained from a match between theory and experiment are summarized in Table II. Section IV D contains the results of electrical Hall effect measurements for chlorine-doped $Zn_{1-x}Mn_xSe$ samples for fixed doping source temperature. Section V summarizes our main findings.

II. GROWTH AND EXPERIMENT

Two series of undoped and chlorine doped $Zn_{1-x}Mn_xSe$ samples with Mn concentrations ranging from 0 to 43% were epitaxially grown on semi-insulating GaAs(001) substrates by molecular-beam epitaxy (MBE). Elemental Zn, Mn, and Se sources were used. The substrate temperature was fixed to 280 °C. For the doped sample series, a $ZnCl_2$ compound source was used for *n*-type doping of the samples. The $Zn_{1-x}Mn_xSe$ layer thickness varies between 170 and 1000 nm. The latter was determined optically by analyzing the Fabry-Pérot fringes in the visible spectral range in room-temperature reflectance spectra, using composition-dependent and wavelength-dependent refractive index data from our previous work.[21] For accurate determination of the manganese content in each sample, we used Rutherford backscattering (RBS), particle-induced x-ray emission (PIXE), energy dispersive x-ray (EDX) analysis, and x-ray diffraction (XRD).[22] The results from all these methods were in reasonable agreement, but the possibility of about ±1% error bar in the manganese concentration determination still cannot be excluded.

The reflectivity of $Zn_{1-x}Mn_xSe$ epilayers was measured over the wave number range from 150 to 5000 cm^{-1} using a Bruker IFS113v Fourier transform spectrometer. Measurements were carried out at an angle of incidence of about 11° with a gold mirror as a reference. Spectra were taken at a resolution of 1 cm^{-1}. In order to improve the signal-to-noise ratio, an average over 100 interferrogram scans was Fourier-transformed for each spectrum. A mercury lamp in combination with a helium cooled Si bolometer detector and a 3.5 -μm-thick mylar beam splitter were employed for the measurements in the far-infrared (FIR) region from 150 to 650 cm^{-1}. In the mid-infrared (MIR) region from 700 to 5000 cm^{-1}, a mercury cadmium telluride (MCT)/KBr detector and a KBr beam splitter were used with a globar (silicon carbide) light source. To cover the small gap from 650 to 700 cm^{-1}, we measured the spectra from 600 to 3000 cm^{-1} using a deuterated tri-glycine sulphate (DTGS)/KBr detector with globar light source and KBr beam splitter. Signal strength and reflectivity accuracy were better in the FIR range than the MIR, so the MIR reflectivity spectra were rescaled to coincide with the FIR reflectivity spectra in the overlapping region.

III. THEORETICAL CONSIDERATIONS

A. Data analysis

Theoretical reflection spectra based on a multioscillator model for optical phonons and a Drude model for free-charge carriers can be calculated. In the normal-incident case, the reflectivity R is given by

$$R = \frac{(n-1)^2 + \kappa^2}{(n+1)^2 + \kappa^2}, \tag{1}$$

where n is a real part of the refractive index and κ is the extinction coefficient. The relation between n and κ is given by the complex dielectric function $\epsilon(\omega) = (n + i\kappa)^2$.

For photon energies well below the band gap, the optical dielectric function in the material arises from the interactions among photons, phonons, and plasmons. For undoped (intrinsic: *i*) semiconductors, the contribution of polar lattice vibrations to the dielectric function can simply be described by using classical harmonic oscillator (HO) functions with Lorentzian-type broadening. Multinary group alloys with multiple IR-active phonon modes require sets of multiple oscillators to model the dielectric function. The classical model for a set of j uncoupled harmonic oscillators can be expressed as

$$\epsilon(\omega) = \epsilon^{L}(\omega) = \epsilon_\infty + \sum_j \frac{F_j \omega_{TO,j}^2}{\omega_{TO,j}^2 - \omega^2 - i\gamma_{TO,j}\omega} \tag{2}$$

with

$$F_j = \epsilon_\infty \frac{\omega_{LO,j}^2 - \omega_{TO,j}^2}{\omega_{TO,j}^2}, \tag{3}$$

were $F_j, \omega_{TO,j}$, and γ_{TOj}, are the strength, resonance frequency, and the broadening values of the jth oscillator, respectively. ϵ_∞ is the high frequency dielectric constant, which includes the contributions from all the interband transitions to the dielectric function. For undoped samples, the only contribution to the dielectric function comes from the lattice atoms, denoted here as $\epsilon^{L}(\omega)$. However, for the case of mixed alloys like $Zn_{1-x}Mn_xSe$, multiple phonon modes with large transverse optical–longitudinal optical (TO-LO) splitting exist. In this case, due to the anharmonicity effects, the simple model presented in Eq. (2) is not sufficient anymore to accurately describe the infrared (IR) reflection data (see, e.g., Refs. 23–25 and references therein). Therefore, for mixed alloys like *i*-$Zn_{1-x}Mn_xSe$ the IR dielectric function is written as a product of individual oscillator terms[24]

$$\epsilon(\omega) = \epsilon^{L}(\omega) = \epsilon_\infty \prod_j \frac{\omega^2 - \omega_{LO,j}^2 + i\gamma_{LO,j}\omega}{\omega^2 - \omega_{TO,j}^2 + i\gamma_{TO,j}\omega}, \tag{4}$$

where $\omega_{TO,j}(\omega_{LO,j})$ and $\gamma_{TO,j}(\gamma_{LO,j})$ are the frequency and broadening values of the jth transverse (longitudinal) optical phonon mode, respectively.[26]

In case of the chlorine-doped $Zn_{1-x}Mn_xSe$ samples, free-charge carriers are present in the medium so the total dielectric function is written as a sum of the lattice contribution $\epsilon^{L}(\omega)$ and the free-carrier (FC) contribution $\epsilon^{FC}(\omega)$

$$\epsilon(\omega) = \epsilon^{L}(\omega) + \epsilon^{FC}(\omega). \quad (5)$$

The free-charge-carrier contribution to the dielectric function $\epsilon^{FC}(\omega)$ is described by the well-known classical Drude equation

$$\epsilon^{FC}(\omega) = -\frac{\omega_p^2}{\omega^2 + i\omega\gamma_p}, \quad (6)$$

where ω_p is the *unscreened*[27] plasma frequency and γ_p the plasma damping constant, respectively. γ_p is equal to the inverse scattering time of the conduction band electrons in the crystal and can therefore also be used to extract the optical resistivity and optical mobility in doped samples.[28]

The optical electron effective mass m_{op}^* at the Fermi energy and the electron mobility μ can be determined from[29]

$$m_{op}^* = \frac{ne^2}{\epsilon_0\omega_p^2} \quad (7)$$

and

$$\mu = \frac{e}{m_{op}^*\gamma_p}, \quad (8)$$

where e is the electronic charge, ϵ_0 is the permittivity of free space, and n is the free-electron concentration, respectively. The free-electron concentration in the mentioned formula was determined using Hall effect measurements.

B. Theoretical calculations of m_{op}^*

From our results (see Sec. IV C), we found that both ZnSe and $Zn_{1-x}Mn_xSe$ show a carrier density dependent electron effective mass due to the conduction band nonparabolicity. The nonparabolic dispersion of the conduction band has been calculated using Kane's $k\cdot p$ perturbation approach.[30] In $Zn_{1-x}Mn_xSe$, for $x=0$ (≈ 0.13), the spin-orbit (SO) splitting, $\Delta_{SO}=0.424$ eV (≈ 0.53 eV) is much smaller than the band gap energy $E_G=2.711$ eV (≈ 2.664 eV).[21] Therefore, we neglected the spin-orbit splitting in our calculations. This approximation is used to estimate the perturbation of the lowest conduction band by the valence bands. Neglecting further perturbations from remote bands, an analytical form of the conduction-band dispersion is obtained by solving Kane's two-band $k\cdot p$ model[30]

$$E_C(k) = E_G + \frac{\hbar^2k^2}{2m_0} + \frac{1}{2}\left(\sqrt{E_G^2 + 4E_P\frac{\hbar^2k^2}{2m_0}} - E_G\right), \quad (9)$$

E_G is the direct band-gap energy (at $k=0$), and E_P is an energy parameter related to the interband momentum matrix element (P),

$$E_P = 2m_0P^2 \quad (10)$$

with

$$P^2 = \frac{1}{2m_0}\left(\frac{m_0}{m_{\Gamma_6}} - 1\right)E_G, \quad (11)$$

where m_0 is the free-electron mass and m_{Γ_6} the effective Γ_6 conduction band-edge mass. The optical electron effective mass determined in our measurements is k dependent and given by

$$m_{op}^*(k) = \frac{\hbar^2k}{dE_C(k)/dk}. \quad (12)$$

The expression for the optical electron effective mass calculated using Eqs. (9)–(12) can be approximately described by

$$\frac{1}{m_{op}^*(k)} = \frac{1}{m_0}\left\{1 + \left(\frac{m_0}{m_{\Gamma_6}} - 1\right) \times \left[1 + \left(\frac{m_0}{m_{\Gamma_6}} - 1\right)\frac{2\hbar^2k_f^2}{m_0E_G}\right]^{-1/2}\right\}, \quad (13)$$

where m_{Γ_6}, the effective Γ_6 conduction band-edge mass, is used as a fit parameter in our calculations. The relation $k_f = (3\pi^2n)^{1/3}$ relates the Fermi wave vector k_f to the free-electron concentration n. Neglecting the thermal broadening of the Fermi distribution, the Fermi level can be approximated (at the Fermi wave vector k_f) using the experimentally determined infrared optical electron effective mass (m_{op}^*) via the following equation:

$$E_f(k) = \frac{\hbar^2k_f^2}{2m_{op}^*(k)}. \quad (14)$$

IV. RESULTS AND DISCUSSION

A. Far-infrared reflectivity: Phonon properties (series of undoped samples)

Microscopic vibrations involving the motion of the atomic nuclei (which are much heavier than the electrons) usually have their resonance frequencies in the infrared region. These characteristic frequencies depend on the oscillating masses and the strength of the bonding between them. Therefore, infrared (IR) spectroscopy is a useful tool to extract information about lattice vibrations, impurities, disorder, and alloy compositions.

Figures 1 and 2 show the temperature-dependent FIR reflectivity spectra for two typical $Zn_{1-x}Mn_xSe/GaAs$ ($x=0$, 0.43) samples measured over the wave-number range from 190 to 320 cm^{-1} at temperatures from 20 to 300 K. Figure 3 compares the FIR reflectivity spectra for several $Zn_{1-x}Mn_xSe/GaAs$ ($x=0$, 0.14, 0.22, 0.43) samples measured at 20 K. For clarity, the spectra are shifted on the reflectivity scale. (The arrows are used to indicate the variation of different features as a function of temperature or Mn contents.) The optical phonon mode frequencies and other parameters extracted from the theoretical fits to the experimental FIR spectra at 20 K (discussed in Sec. III A) are collected in Table I.

It should be noted from Table I that for the $Zn_{1-x}Mn_xSe$ samples with low Mn contents ($x=0$, 7.94%) the equal values for the transverse optical (TO) and longitudinal optical (LO) broadenings (γ) are found. For such cases, the usual sum of contributions to the dielectric functions would also be sufficient.[31] However, for the samples with larger Mn contents, the differences between LO and TO broadenings be-

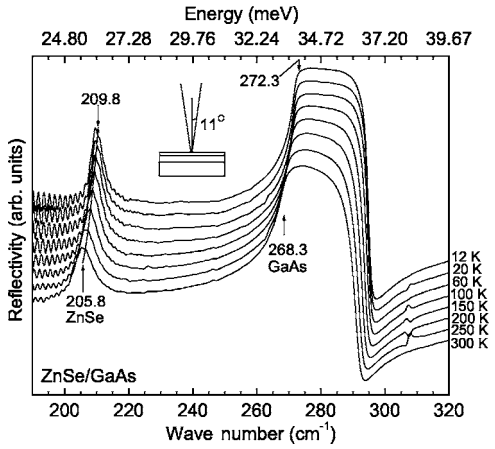

FIG. 1. Temperature-dependent far-infrared reflection spectra for an undoped ZnSe/GaAs sample. These measurements were performed at an angle of incidence of about 11°.

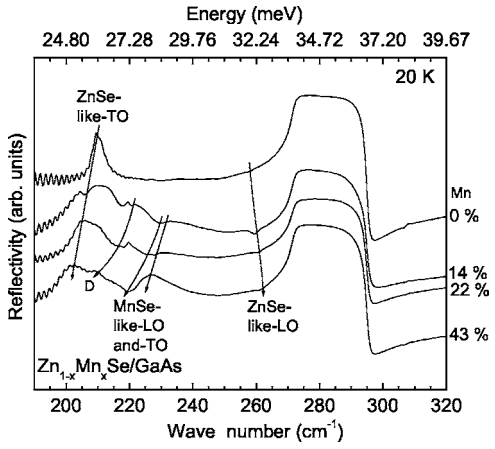

FIG. 3. Far-infrared reflection spectra for nominally undoped $Zn_{1-x}Mn_xSe/GaAs$ (x=0, 0.14, 0.22, 0.43) samples at 20 K. The arrows are used to guide the eye.

come significant and the anharmonicity effects discussed in Sec. III A play a larger role and have to be taken into account to model the experimental data accurately.

In Fig. 1, the FIR reflectivity spectrum for the ZnSe/GaAs sample shows two phonon features: ZnSe and GaAs phonons at 205.8 and 268.3 cm^{-1}, respectively (300 K). At 20 K, the TO-phonon frequency (ω_{TO}) of both ZnSe and GaAs phonons shows a blueshift of about 4 cm^{-1}. This particular sample contains a 172-nm-thin epilayer of *i*-ZnSe deposited on an *i*-GaAs substrate. It is interesting to note the thickness effect on the shape of the reststrahlen band for the ZnSe phonon. This aspect is discussed in more detail in Sec. IV B.

The inset in Fig. 1 shows the typical structure of our samples studied in this work. We used a three-layer model to analyze our data. This model consists of the GaAs substrate, the $Zn_{1-x}Mn_xSe$ layer (170–1000 nm) and a very thin (5 nm) ZnSe cap layer, which was deposited to prevent oxidation of the $Zn_{1-x}Mn_xSe$ layer.

For the case of $Zn_{0.57}Mn_{0.43}Se/GaAs$ (Fig. 2), there are even at room temperature three clear phonon features at 200, 220.8, and 268.3 cm^{-1} attributed to ZnSe-like, MnSe-like, and GaAs-like phonons, respectively. At 20 K, the ω_{TO} of ZnSe-like, MnSe-like, and GaAs-like phonons shows a blueshift of about 3.7, 3.8, and 4 cm^{-1}, respectively. In addition to the known ZnSe-like and MnSe-like phonon resonances, we observe a weak feature below the MnSe-like phonon band, labeled *D* in Figs. 2 and 3. With increasing Mn concentration (see Fig. 3), the frequency of this feature shows a redshift comparable to that of the other phonons. From Fig. 2, we notice clearly that as the temperature decreases to 20 K, the frequency of this weak feature also shifts to higher frequencies like the other phonon features. This observation excludes the possibility for the *D* feature to be an experimental artifact. We suggest that the additional feature observed in our measurements is a weak mode, which has its origin in the alloy disorder resulting from the Mn incorporation in the samples. The alloy disorder in the samples leads to the spatial composition fluctuations resulting in clustering or formation of Mn-related complexes. These microscopic changes in the neighboring environment can result in such weak-mode features.[32,33]

Figure 4 shows the variation of ω_{TO} and ω_{LO} as a function

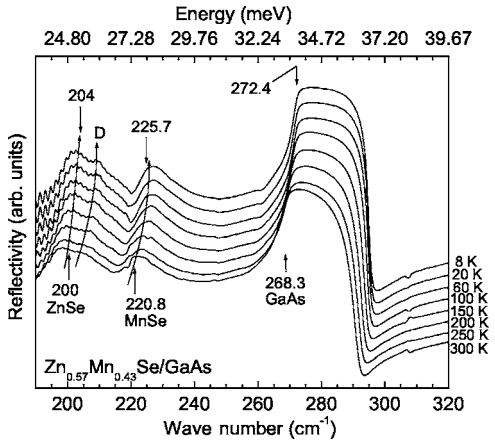

FIG. 2. Temperature-dependent far infrared reflection spectra for an undoped $Zn_{0.57}Mn_{0.43}Se/GaAs$ sample. The arrows are used to guide the eye.

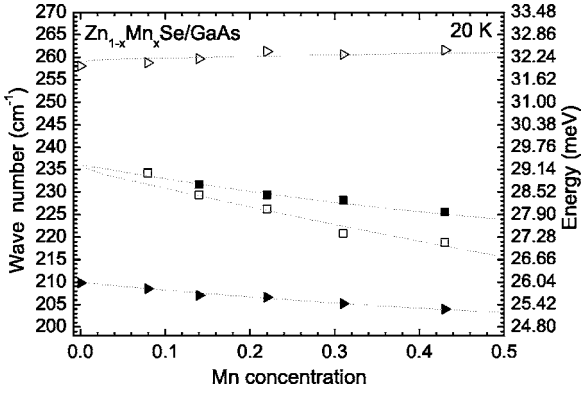

FIG. 4. Variation of optical phonon mode frequencies as a function of Mn content extracted from theoretical fits to the experimental FIR reflection data (T=20 K). The dotted lines are used to guide the eye. Symbols are described in the text.

TABLE I. ZnSe-like and MnSe-like phonon mode parameters extracted from theoretical fittings using Eq. (4).

		ZnSe-like mode				MnSe-like mode			
Sample	Mn (%)	$\omega_{TO}(cm^{-1})$	$\omega_{LO}(cm^{-1})$	$\gamma_{TO}(cm^{-1})$	$\gamma_{LO}(cm^{-1})$	$\omega_{TO}(cm^{-1})$	$\omega_{LO}(cm^{-1})$	$\gamma_{TO}(cm^{-1})$	$\gamma_{LO}(cm^{-1})$
1	0	209.8	258.1	1.6	1.6				
2	7.94	208.5	258.8	2.51	2.51	234.43	234.17	2.55	2.55
3	14	207.04	259.7	4.55	4	231.75	229.95	7.41	7.41
4	22	206.62	261.3	5.03	4.47	229.36	226.27	8.52	7.97
5	31	205.18	260.65	5	3.5	228.21	220.84	11.12	6.95
6	43	203.95	261.6	8	3.57	225.69	218.85	7.23	10

of Mn content extracted from fits to our FIR reflection data measured at 20 K. The triangles (squares) are used for the ZnSe-like (MnSe-like) phonon modes. The solid (empty) symbols represent the TO (LO) modes. ZnSe-like TO and MnSe-like TO frequencies both shift continuously toward lower wave numbers with increasing Mn concentration. However, the ZnSe-like LO frequency shifts only very little toward higher wave numbers with increasing Mn concentration. (The dotted lines are used to guide the eye.) According to the extended classification scheme for the optical phonon modes in mixed alloys (Genzel *et al.*[34]), the observed behavior in our $Zn_{1-x}Mn_xSe$ series of samples ($0 \leqslant x \leqslant 0.43$) corresponds to an "intermediate-mode" behavior. A similar behavior for $Zn_{1-x}Mn_xSe$ mixed crystals was also observed in previous studies.[15–19]

B. Thickness effects in layered media

Figure 5 demonstrates the effect of the layer thickness on the shape of the reststrahlen band. It compares the simulated FIR reflectivity spectra for an undoped ZnSe/GaAs sample with different ZnSe layer thicknesses. The experimental spectra for cases (a) and (b) are represented by circles. In the simulation, the ω_{TO} and ω_{LO} frequencies for ZnSe at 20 K are taken to be 210 and 257 cm^{-1}, respectively. It is interesting to note, how the reststrahlen band of ZnSe phonon changes its shape depending on ZnSe layer thickness.

This effect can be understood with the help of the imaginary part of the refractive index. Without damping, κ has a singularity at the transverse optical (TO) phonon frequency ω_{TO} and decays strongly toward the longitudinal optical (LO) phonon frequency ω_{LO} (see inset). Consequently in the reststrahlen band region, the evanescent wave has a short penetration depth l_p close to the ω_{TO} frequency. The penetration depth l_p is related to the extinction coefficient κ via the following relation:

$$l_p = \left[\kappa(\omega) \frac{\omega}{c} \right]^{-1}, \tag{15}$$

where ω is the frequency and c is the velocity of light in vacuum. l_p increases strongly towards the longitudinal optical (LO) phonon frequency ω_{LO}. As a result, in the reststrahlen band, the reflectivity will be high in the spectral region where the sample thickness d is larger than the penetration depth ($d > l_p$). For the spectral ranges where the sample thickness d is shorter than the penetration depth ($d < l_p$), the resulting reflectivity will be lower since for ($d < l_p$), the evanescent wave reaches the substrate below the

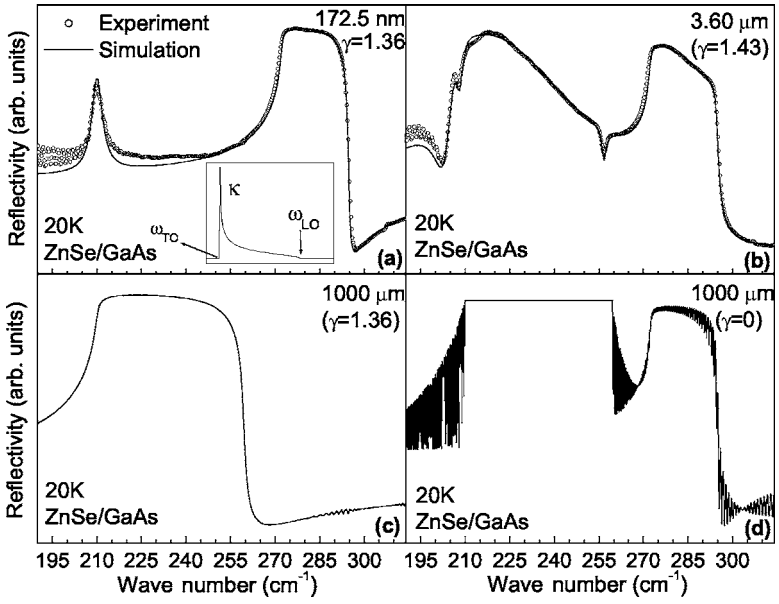

FIG. 5. Simulated far-infrared reflection spectra for undoped ZnSe/GaAs samples with different ZnSe layer thicknesses and damping. The experimental reflection spectra for case (a) and (b) are shown by circles. The inset shows schematically the imaginary part of the refractive index.

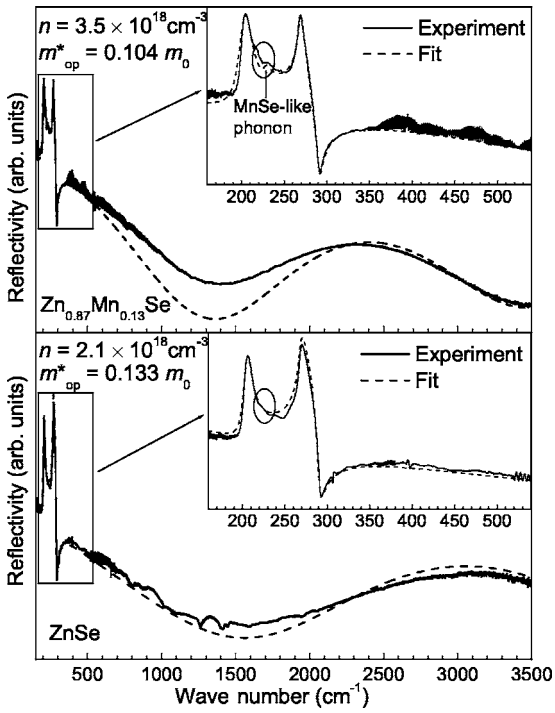

FIG. 6. Plasma edge observed in the room-temperature infrared reflectivity spectra of *n*-type $Zn_{0.87}Mn_{0.13}Se:Cl$ and ZnSe:Cl samples. The dashed line is a fit to the experimental points using reflectivity spectra calculated with Eqs. (1) and (5). The inset shows the spectral region around the ZnSe-like, MnSe-like and GaAs-like phonons.

top layer and continues to propagate in the substrate in an oscillatory fashion.

Therefore, this effect can easily be seen in samples with a thin ZnSe layer resulting in a narrow reststrahlen band, e.g., case (a). If the ZnSe layer is thick enough ($d > l_p$) to provide enough medium for evanescent wave propagation in the ZnSe layer, e.g., case (c), then a full ZnSe reststrahlen band can be observed. In case (c), the GaAs reststrahlen band has disappeared due to damping ($\gamma = 1.36$) in the ZnSe layer. In the ideal situation of zero damping ($\gamma = 0$), e.g., case (d), full reststrahlen bands of ZnSe and GaAs can be observed. The narrow oscillations in case (d) are the Fabry-Pérot fringes due to the very large ZnSe layer thickness (1000 μm) used in the simulation. In case (d), the reflectivity slightly above ZnSe-ω_{LO} does not go completely to zero due to the contribution coming from the underlying GaAs substrate.

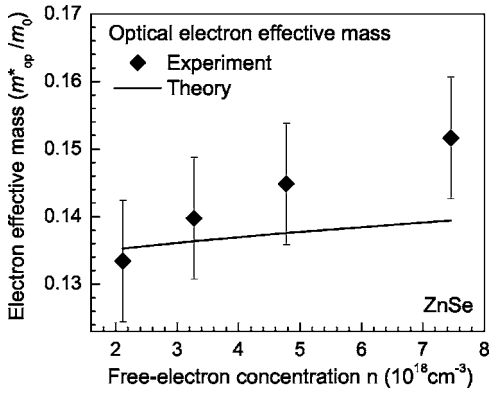

FIG. 7. Optical electron effective mass (m^*_{op}) as a function of free-electron concentration for *n*-type ZnSe:Cl samples.

C. Plasma edge reflectivity: Determination of electron effective mass (series of doped samples with ≈13 % Mn)

To extract some information about the electron effective mass, we studied a series of *n*-type Zn(Mn)Se:Cl bulk layers, with free-electron concentrations ranging from 1.0×10^{18} cm^{-3} to 8.0×10^{18} cm^{-3}. All doped $Zn_{1-x}Mn_xSe$ samples ($0 \leqslant x \leqslant 0.13$) investigated in this section had the zinc-blende structure, in agreement with the results of Kolodziejski *et al.*[35] The free-electron concentration in our samples was determined using Hall measurements (see Sec. IV D). The experimental electron effective mass was extracted from reflectivity data by making a fit using the Drude-Lorentz model described in Sec. III A.

Figure 6 shows the room-temperature infrared reflectivity measurement (solid line) and theoretical fit (dashed line) of a $Zn_{0.87}Mn_{0.13}Se:Cl$ and a ZnSe sample with free-electron concentration (optical mobility) of 3.5×10^{18} cm^{-3} (155 cm^2 V^{-1} s^{-1}) and 2.1×10^{18} cm^{-3} (295 cm^2 V^{-1} s^{-1}), respectively. The inset clearly shows the presence of ZnSe-like and GaAs-like phonons at 203 and 269 cm^{-1}, respectively. In case of the $Zn_{0.87}Mn_{0.13}Se$ sample, there is another very weak feature at 228 cm^{-1}, attributed to the MnSe-like phonon. The data for these samples resulted in optical electron effective masses of $0.104 \pm 0.009\ m_0$ (13% Mn) and $0.133 \pm 0.009\ m_0$ (0% Mn), respectively, where m_0 is the free-electron mass. The plasma reflection edge is very broad due to the low electron mobility in these samples.

Figures 7 and 8 summarize the optical electron effective masses m^*_{op} as a function of free-electron concentration for *n*-type ZnSe:Cl and $Zn_{1-x}Mn_xSe:Cl$ ($x = 0.10$, 0.105, 0.115, and 0.13) samples, respectively. We note that the optical electron effective mass values for $Zn_{1-x}Mn_xSe$ are lower than for ZnSe. The solid line represents the calculated m^*_{op} values obtained from Eq. (13) given in Sec. III B with the Γ_6 conduction-band-edge mass as an input fit parameter.[36] For calculations, we used the $Zn_{1-x}Mn_xSe$ band-gap energy $E_G = 2.71$ eV (2.664 eV) for $x = 0\%$ (13%), respectively.[21] Both experimental and calculated electron effective masses increase as a function of free-carrier density. However, the increase in the calculated electron effective mass is less pronounced than is found in experiment. This may be due to the fact that in our calculations we neglected the increase in the effective Γ_6 conduction-band-edge mass with increasing free-electron concentration.[37–39] The carrier density dependent electron effective mass in ZnSe and $Zn_{1-x}Mn_xSe$ provides information about the nonparabolicity of the conduction-band dispersion.[40,41]

From our theoretical modeling (see Sec. III B), we estimate the extrapolated room-temperature band-edge electron mass (m_{Γ_6}) in ZnSe and $Zn_{0.87}Mn_{0.13}Se$ to be about 0.132 m_0 and 0.093 m_0, respectively (within about ±9% accuracy). The former value is in good agreement with the previously reported conduction-band-edge masses[42–45] listed in Table II.

TABLE II. Conduction-band-edge masses.

	ZnSe	$Zn_{0.87}Mn_{0.13}Se$
This work	0.132 m_0	0.093 m_0
Reference 42	0.140 m_0 (at 0 K)	
Reference 43	0.130 m_0	
Reference 44	0.135 m_0 (at 4.2 K)	
Reference 45	0.137 m_0	

To our knowledge, no reported value seems to be available for the electron effective mass in $Zn_{1-x}Mn_xSe$. However, preliminary magneto-ellipsometric measurements[46] suggest a m^*_{op} value of 0.107 m_0 for $Zn_{0.90}Mn_{0.10}Se$ at a carrier density of 6.0×10^{18} cm^{-3}, in good agreement with our results.

Figure 9 compares the shift of the electron Fermi level as a function of free-electron concentration for ZnSe and $Zn_{0.87}Mn_{0.13}Se$ samples. As expected, the electron Fermi level is higher for similar electron concentrations due to the lower electron effective mass in $Zn_{0.87}Mn_{0.13}Se$.

The optical mobility and electron effective mass extracted from infrared studies of doped samples are listed in Table III. The comparison between the optical and electrical mobilities is presented in Sec. IV D.

D. Hall effect measurements: Free-electron concentration and mobility (series of doped samples)

The free-charge-carrier concentration and the Hall mobility were determined by room-temperature Hall and conductivity measurements in the van der Pauw configuration using a magnetic field of 0.9 T. The obtained free-electron concentrations, Hall mobilities, and resistivities are listed in Table III. Mn incorporation into ZnSe not only reduces the electron effective mass but also influences its maximum dopability limit.[47] The incorporation of Mn increases the electrical resistivity and decreases the mobility due to the increasing scattering rates and the decreasing carrier concentration.[48]

Figure 10 shows the effect of Mn incorporation on the free-electron concentration. At constant $ZnCl_2$ doping source temperature (190 °C), the free-electron concentration decreases continuously with increasing Mn content in the sample. If more Mn is incorporated in the samples with constant $ZnCl_2$ effusion cell temperature, the doping concentration is expected to slightly decrease due to the resulting increase in the growth rate. However, we found that the incorporation of only 30% Mn causes a very strong reduction in the free-electron concentration, much higher than the expected influence of the growth rate. A similar behavior, studied for limited Mn concentrations of up to 11% was also reported elsewhere.[49] This drastic decrease in free-electron concentration is due to the formation of Mn-related defect complexes.

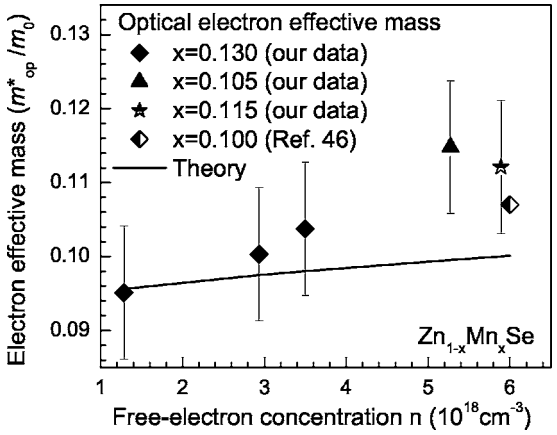

FIG. 8. Optical electron effective mass (m^*_{op}) as a function of free-electron concentration for n-type $Zn_{1-x}Mn_xSe$:Cl epilayer samples.

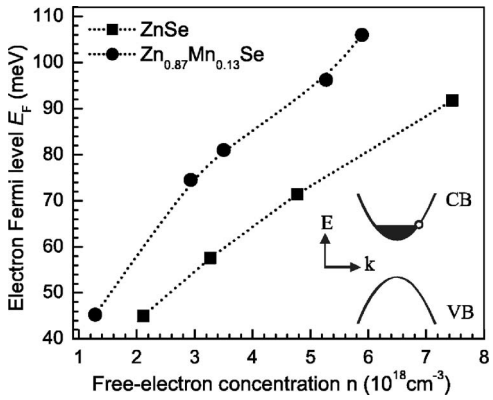

FIG. 9. Shift of the electron Fermi level as a function of free-electron concentration calculated using (14), Sec. III B. The inset shows schematically the point at which the m^*_{op} is measured for a particular Fermi level in the conduction band (CB).

Figure 11 compares the reciprocal room-temperature Hall and infrared mobilities [extracted from Eq. (8)] as a function of the free-electron concentration for ZnSe. The mobility resulting from scattering at ionized impurities μ_i is related to the ionized impurity density N_I via the proportionality equation[50]

$$\mu_i \propto (m^*)^{-1/2} N_I^{-1} T^{3/2}, \tag{16}$$

where T is the temperature and m^* the effective mass, respectively. At room temperature, most impurities are ionized.

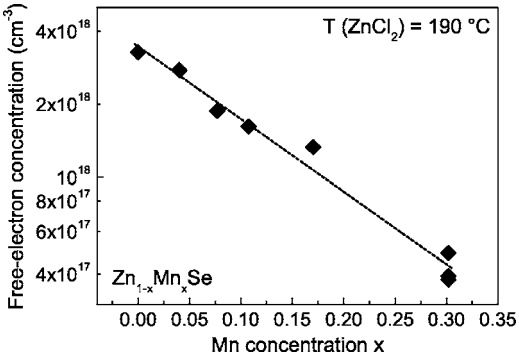

FIG. 10. Room-temperature free-electron concentrations for the samples grown with a fixed $ZnCl_2$ source temperature but with different Mn contents.

TABLE III. Mn content, free-electron concentration, Hall and infrared mobility, resistivity, and optical electron effective mass for different MBE-grown chlorine doped $Zn_{1-x}Mn_xSe$:Cl epitaxial films.

Sample	Mn (%)	$n(10^{18}\text{cm}^{-3})$	$\mu_{\text{Hall}}(\text{cm}^2/\text{V-S})$	$\mu_{\text{IR}}(\text{cm}^2/\text{V-S})$	$\rho_{\text{Hall}}(10^{-3}\ \Omega\ \text{cm})$	$\rho_{\text{IR}}(10^{-3}\ \Omega\ \text{cm})$	m^*_{op}/m_0 (IR)
1	0	2.11	363	295	8.14	9.98	0.1334
2	0	3.27	318	223	6.0	8.56	0.140
3	0	4.77	273	205	4.79	6.38	0.145
4	0	7.45	286	224	2.93	3.74	0.152
5	12.8	1.28	161	151	30.2	32.2	0.095
6	13.1	2.93	145	131	14.7	16.2	0.100
7	12.7	3.50	180	155	9.88	11.5	0.104
8	10.5	5.27	161	138	7.37	8.58	0.115
9	11.5	5.89	155	136	6.85	7.8	0.112
10	10.0	6.0	92		1.13		0.107[a]

[a]Reference 46.

Both reciprocal mobilities ($\mu_{\text{IR}}^{-1}, \mu_{\text{Hall}}^{-1}$) increase with increasing doping concentration, as predicted by (16). At very high doping concentrations, this behavior seems to saturate. The optical mobility is found to be lower than the electrical Hall mobility, roughly by a factor of 0.7. Such a difference in optical and electrical mobilities was also observed for other materials.[51–53]

V. CONCLUSIONS

In conclusion, we investigated the phonon and free-charge carrier properties in undoped and doped series of $Zn_{1-x}Mn_xSe$ samples grown by molecular-beam epitaxy. The far-infrared reflection studies performed on series of undoped $Zn_{1-x}Mn_xSe$ samples suggest an intermediate-mode behavior for the optical phonon modes in the composition range $0 \leqslant x \leqslant 0.43$. In addition to the known ZnSe-like and MnSe-like phonon resonances, we also observed a weak-mode feature below the MnSe-like phonon band. This additional feature shows a temperature and Mn concentration dependent redshift. We suggest that this weak mode has its origin in the disorder resulting from the Mn incorporation in the samples. From room-temperature plasma edge measurements carried out on chlorine-doped *n*-type $Zn_{1-x}Mn_xSe$ epilayers ($0 \leqslant x \leqslant 0.13$) and from their theoretical fittings using the Drude-Lorentz multioscillator model, we extracted the optical electron effective mass (m^*_{op}) in doped Zn(Mn)Se:Cl samples with different Mn contents and free-electron concentrations. A distinct reduction of the electron effective mass in $Zn_{1-x}Mn_xSe$ is observed with increasing Mn content. ZnSe and $Zn_{1-x}Mn_xSe$ both show a carrier density dependence of the electron effective mass due to the nonparabolic nature of the conduction band. From our theoretical modeling, we determined the extrapolated room-temperature band-edge electron mass in ZnSe and $Zn_{0.87}Mn_{0.13}Se$ to be about 0.132 m_0 and 0.093 m_0, respectively (within about ±9% accuracy). The optical mobility and resistivity are found to decrease with increasing free-electron concentration in ZnSe samples. From room-temperature Hall effect measurements on chlorine-doped $Zn_{1-x}Mn_xSe$ samples, we found a drastic reduction in the free-electron concentration with increasing Mn content. The incorporation of Mn increases the resistivity and decreases the mobility of the free-charge carriers in the samples. The knowledge about the influence of Mn on the conduction-band-edge mass and the electrical properties like free-electron concentration, mobility, and resistivity will be beneficial for utilizing ZnSe-based materials in device applications.

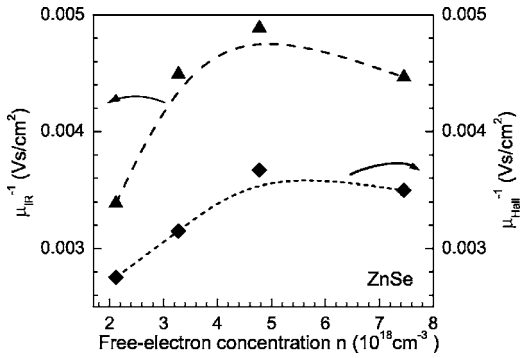

FIG. 11. Reciprocal room-temperature optical and electrical mobility vs free-electron concentration for ZnSe samples measured by Hall effect (diamond) and IR reflection measurements (triangles). The dashed lines are used to guide the eye.

ACKNOWLEDGMENTS

This work was supported by the Deutsche Forschungsgemeinschaft (DFG) within the Graduiertenkolleg "Kollektive Phänomene im Festkörper" (GK 284) and the Center for Functional Nanostructures (CFN) at the University of Karlsruhe (project A2). The authors acknowledge D. Spemann (University of Leipzig, Germany) for RBS and PIXE measurements, P. Pfundstein and D. Gerthsen at the Laboratory for Electron Microscopy (University of Karlsruhe, Germany) for EDX measurements, as well as T. Hofmann and M. Schubert (University of Leipzig, Germany) for magnetoellipsometric investigations.

*Electronic address: kapil.agarwal@physik.uni-karlsruhe.de

[1] M. A. Haase, J. Qiu, J. M. DePuydt, and H. Cheng, Appl. Phys. Lett. **59**, 1272 (1991).
[2] M. Klude and D. Hommel, Appl. Phys. Lett. **79**, 2523 (2001).
[3] H. Luo and J. Furdyna, Semicond. Sci. Technol. **10**, 1041 (1995).
[4] H. Babucke, P. Thiele, T. Prasse, M. Rabe, and F. Henneberger, Semicond. Sci. Technol. **13**, 200 (1998).
[5] H. Ishikura, T. Abe, N. Fukuda, H. Kasada, and K. Ando, Appl. Phys. Lett. **76**, 1069 (2000).
[6] O. Goede and W. Heimbrodt, Phys. Status Solidi B **146**, 11 (1988).
[7] J. K. Furdyna, J. Appl. Phys. **64**, R29 (1988).
[8] J. Stankiewicz and J. R. Fermín, J. Appl. Phys. **63**, 3300 (1988).
[9] N. Dai, H. Luo, F. C. Zhang, N. Samarth, M. Dobrowolska, and J. K. Furdyna, Phys. Rev. Lett. **67**, 3824 (1991).
[10] J. C. Egues, Phys. Rev. Lett. **80**, 4578 (1998).
[11] R. Fiederling, M. Keim, G. Reuscher, W. Ossau, G. Schmidt, A. Waag, and L. W. Molenkamp, Nature (London) **402**, 787 (1999).
[12] B. T. Jonker, Y. D. Park, B. R. Bennett, H. D. Cheong, G. Kioseoglou, and A. Petrou, Phys. Rev. B **62**, 8180 (2000).
[13] M. Oestreich, Nature (London) **402**, 735 (1999).
[14] D. Tröndle, W. Löffler, Th. Passow, B. Daniel, M. Grün, M. Hetterich, C. Klingshirn, and H. Kalt, in *Proceedings of CLEO (Conference on Lasers and Electro-Optics)/QELS (Quantum Electronics and Laser Science Conference), 2005, Paper No.* JTuC96 (Optical Society of America, Washington, DC, 2005).
[15] P. D. Lao, Yile Guo, G. G. Siu, and S. C. Shen, Phys. Rev. B **48**, 11701 (1993).
[16] A. K. Arora, E-K. Suh, U. Debska, and A. K. Ramdas, Phys. Rev. B **37**, 2927 (1988).
[17] Cheng-Tzung Tsai, Der-san Chuu, Jiun-Yueh Leou, and Wu-Ching Chou, Jpn. J. Appl. Phys., Part 1 **36**, 4427 (1997).
[18] T. R. Yang, C. C. Lu, W. C. Chou, Z. C. Feng, and S. J. Chua, Phys. Rev. B **60**, 16058 (1999).
[19] W. Lu, P. L. Liu, G. L. Shi, S. C. Shen, and W. Giriat, Phys. Rev. B **39**, 1207 (1989).
[20] Landolt-Börnstein, in *Numerical Data and Functional Relationships in Science and Technology*, edited by U. Rössler, Vol. III/41B (Springer, Berlin, 1999).
[21] J. Kvietkova, B. Daniel, M. Hetterich, M. Schubert, D. Spemann, D. Litvinov, and D. Gerthsen, Phys. Rev. B **70**, 045316 (2004).
[22] M. Hetterich, B. Daniel, C. Klingshirn, P. Pfundstein, D. Litvinov, D. Gerthsen, K. Eichhorn, and D. Spemann, Phys. Status Solidi C **1**, 649 (2004).
[23] F. Gervais and B. Piriou, J. Phys. C **7**, 2374 (1974).
[24] F. Gervais and B. Piriou, Phys. Rev. B **10**, 1642 (1974).
[25] F. Gervais and B. Piriou, Phys. Rev. B **11**, 3944 (1975).
[26] For the case of the chlorine-doped $Zn_{1-x}Mn_xSe$ samples ($x \approx 0.13$), the dominant effect comes from the free-charge carriers so the use of Eq. (2) instead of Eq. (4) does not make any significant difference on the plasma frequency and plasma damping constant.
[27] It should be noted that the definition of the *screened* plasma frequency often used in literature differs from the definition of the *unscreened* plasma frequency ω_p by a factor of $1/\sqrt{\epsilon_\infty}$.
[28] P. Y. Yu and M. Cardona, *Fundamentals of Semiconductors* (Springer, Berlin, 1996).
[29] C. Kittel, *Introduction to Solid State Physics*, 6th ed. (Wiley, New York, 1986).
[30] E. O. Kane, J. Phys. Chem. Solids **1**, 249 (1957).
[31] It should be noted that for the special case of TO and LO broadenings being equal, the product in Eq. (4) becomes equal to the sum in Eq. (2).
[32] M. I. Alonso and K. Winer, Phys. Rev. B **39**, 10056 (1989).
[33] H. W. Verleur and A. S. Barker, Jr., Phys. Rev. **149**, 715 (1966).
[34] L. Genzel, T. P. Martin, and C. H. Perry, Phys. Status Solidi B **62**, 83 (1974).
[35] L. A. Kolodziejski, R. L. Gunshor, T. C. Bonsett, R. Venkatasubramanian, S. Datta, R. B. Bylsma, W. M. Becker, and N. Otsuka, Appl. Phys. Lett. **47**, 169 (1985).
[36] We assumed that the two-band Kane model can be used to roughly estimate the electron effective mass in $Zn_{1-x}Mn_xSe$ alloys.
[37] D. M. Szmyd, P. Porro, A. Majerfeld, and S. Lagomarsino, J. Appl. Phys. **68**, 2367 (1990).
[38] Szmyd and the co-authors (Ref. 37) found that in highly doped samples the effective Γ_6 conduction-band-edge mass also increases resulting from the perturbation caused by donor atoms.
[39] Another reason may be the simplified form of Kane's model used in the theoretical calculations.
[40] K. C. Agarwal, B. Daniel, P. Feinäugle, C. Klingshirn, and M. Hetterich, *Proceedings of Photonics 2004: 7th International Conference on Optoelectronics, Fiber Optics and Photonics, Cochin, India* (2004), Paper No. OMDP9 (unpublished).
[41] K. C. Agarwal, B. Daniel, M. Grün, P. Feinäugle, C. Klingshirn, and M. Hetterich, Appl. Phys. Lett. **86**, 181907 (2005).
[42] P. Lawaetz, Phys. Rev. B **4**, 3460 (1971).
[43] C. S. Wang and B. M. Klein, Phys. Rev. B **24**, 3393 (1981).
[44] T. Ohyama, E. Otsuka, T. Yoshida, M. Isshiki, and K. Igaki, Jpn. J. Appl. Phys., Part 1 **23**, L382 (1984).
[45] Y. Imanaka, N. Miura, and H. Kukimoto, Phys. Rev. B **49**, 16965 (1994).
[46] T. Hofmann and M. Schubert (unpublished).
[47] B. Daniel, K. C. Agarwal, C. Klingshirn, and M. Hetterich, in *Physics of Semiconductors*, edited by J. Menéndez and C. G. Van de Walle, American Institute of Physics Conf. Proc. No. 772 (AIP, New York, 2005), p. 171.
[48] B. Daniel, K. C. Agarwal, J. Lupaca-Schomber, C. Klingshirn, and M. Hetterich, Appl. Phys. Lett. **87**, 212103 (2005).
[49] H. Abad, B. T. Jonker, W. Y. Yu, S. Stoltz, and A. Petrou, Appl. Phys. Lett. **66**, 2412 (1995).
[50] S. M. Sze, *Physics of Semiconductor Devices*, 2nd ed. (Wiley, New York, 1981), pp. 28–29.
[51] H. Z-F. Li, W. Lu, H-J. Ye, Z-H. Chen, X-Z. Yuan, H-F. Dou, and S-C. Shen, J. Appl. Phys. **86**, 2691 (1999).
[52] T. Kozawa, T. Kachi, H. Kano, Y. Taga, M. Hashimoto, N. Koide, and K. Manabe, J. Appl. Phys. **75**, 1098 (1994).
[53] G. Irmer, V. V. Toporov, B. H. Bairamov, and J. Monecke, Phys. Status Solidi B **119**, 595 (1983).